ACS OMEGA

http://pubs.acs.org/journal/acsodf

Article

Micromixer with Fine-Tuned Mathematical Spiral Structures

Binfeng Yin,* Wenkai Yue, A. S. M. Muhtasim Fuad Sohan, Teng Zhou, Changcheng Qian, and Xinhua Wan

Cite This: *ACS Omega* 2021, 6, 30779−30789

Read Online

ACCESS | Metrics & More | Article Recommendations | Supporting Information

ABSTRACT: Micromixers with the microchannel structure can enable rapid and efficient mixing of multiple types of fluids on a microfluidic chip. Herein, we report the mixing performance of three passive micromixers based on the different mathematical spiral structures. We study the fluid flow characteristics of Archimedes spiral, Fermat spiral, and hyperbolic spiral structures with various channel widths and Reynolds number (Re) ranging from 0 to 10 via numerical simulation and visualization experiments. In addition, we analyze the mechanism of streamlines and Dean vortices at different cross sections during fluid flows. As the fluid flows in the Fermat spiral channel, the centrifugal force induces the Dean vortex to form a chaotic advection, enhancing the fluid mixing performance. By integrating the Fermat spiral channel into a microfluidic chip, we successfully detect acute myocardial infarction (AMI) marker with the double-antibody sandwich method and reduce the detection time to 10 min. This method has a low reagent consumption and a high reaction efficiency and demonstrates great potential in point-of-care testing (POCT).

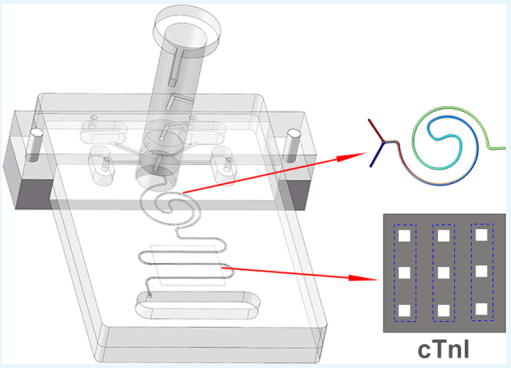

1. INTRODUCTION

Micromixers[1] occupy a vital position in the sample pretreatment of biochemical assays testing.[2] Micromixers is a microdevice with small size, low reagent[3] consumption, and high reaction efficiency.[4] These features enable rapid fluid mixing and analysis. Studies show that the mixing of fluids is crucial for biological and chemical reactions.[5,6] However, laminar fluid mixing is an inefficient process.[7,8] It mainly depends on the diffusion of molecules, especially at low flow rates. Researchers proposed various micromixer structures based on fluid drive methods to enhance fluid mixing and meet experimental requirements.

Micromixers are divided into active and passive mixers depending on different sampling methods.[9−11] Active mixers rely on external energy co-driven fluid flows like electromagnetic drive,[12−14] electric drive,[15,16] mechanical stirring,[17] and thermal expansion.[18,19] This type of mixer has a faster sampling speed and has higher mixing efficiency. Nevertheless, the common disadvantage of active micromixers is their relatively complex structure and relatively high analytical costs. In contrast, passive micromixers are simple in structure and do not require external energy.[20−22] Passive micromixer relies only on the various designs of the microchannels to achieve fluid mixing. Moreover, the small size of this micromixer reduces the cost of analysis. Lok et al.[23] introduced chemiluminescence (CL) detection using a double spiral channel micromixer. It facilitates the mixing of reagents. Experiments prove that the CL signal is double when using a double spiral channel micromixer than a single spiral channel. Furthermore, the micromixer improved the signal by 1.5 times. Yang et al.[24] optimized the settings of a new double spiral channel three-dimensional (3D) micromixer based on the Dean effect principle using hydrodynamic software. The centrifugal force of the double spiral channel micromixer induced the generation and enhancement of Dean vortices to exhibit high mixing efficiency. The Dean vortex can improve fluid's mixing performance and also effectively focus particles or cells of various sizes in the inertial microfluid using the principle of the Dean vortex effect.[25−27] Hossain et al.[28] carried out a numerical study of the mixing performance of a nonaligned input serpentine mixer. It has a higher mixing index than the T-joint inlet micromixer at different Re. Nonaligned input serpentine micromixer induces the lateral flow of the fluid, which expands the contact area between the fluids and enhances the fluid mixing. Vatankhah et al.[29] studied the spiral micromixer using numerical simulation methods. The fluid flowing in the spiral microchannel induces transverse Dean vortices through centrifugal force and enhances the mixing effect of fluids. Wang et al.[30] proposed a serpentine micromixer using elliptical curves, where the Dean vortices induced using different elliptic curves vary continuously with the curvature.

Received: September 11, 2021
Accepted: October 21, 2021
Published: November 2, 2021

The greater the curvature, the stronger the Dean vortices induced, thus improving the mixing performance. Yin et al.[31] reported a microfluidic chip-based magnetic relaxation switched immunosensor based on a snake-shaped mixing channel that mixed MBs-Ab1, CAT-PS-Ab2, and analytes well. This sensor detects α-fetoprotein in actual samples with a 0.56 ng/ml detection limit superior to conventional enzyme-linked immunoassay assays (ELISA).[32−36] The microfluidic chip with mixed channels can integrate into a small portable point-of-care testing (POCT) device.[37−40] It can detect multiple targets or different samples that are well mixed and reacted in the channels. This POCT device expects practical implementation in the community and other settings with its fast detection speed and high sensitivity[41] in chemiluminescent immunoassays.[42]

At present, most micromixers are mainly used for mixing fluids under a high Re (10−100). The mixing of fluids under a low Re (0−10) requires continuous improvement of the structure of the micromixers. Changing the structure of the passive mixer enhances the mixing of the fluid simultaneously, placing higher demands on the fabrication of the chip mold. The complex steps of the conventional photolithography process and extended cycle times make the chip mold fabrication process prone to various defects. These problems are challenging for laboratories with limited facilities. In contrast, the 3D printing technology has convenient and straightforward steps to achieve chip fabrication, which overcomes such drawbacks.[43−46]

Therefore, we investigate the effect of three different spiral structures with varying widths of the channel and different Re (0−10) on mixing the micromixer. Our study is based on numerical simulations[47] and visualization experiments.[48] We also used a Fermat spiral structure as the micromixer for chemiluminescent immunoassay. We injected cardiac troponin and detection antibody conjugated with horseradish peroxidase[49] into the chip under different Re. After mixing and reacting in the spiral channel, it binds to the capture antibody precoated in the detection zone. Under chaotic advection,[50] the micromixer controls the detection time to 10 min and has high sensitivity in detecting cTnI. The introduction of the spiral channel saves valuable time for POCT device testing and has frontier use in POCT devices to diagnose acute myocardial infarction (AMI).

2. EXPERIMENTAL SECTION

2.1. Materials and Equipment. Cardiac troponin I (cTnI), capture antibody (cTnI-Ab1), and detection antibody-conjugated horseradish peroxidase (cTnI-HRP-Ab2) were purchased from Abcam (U.K.). Phosphate-buffered solution (PBS) tablets were from Amresco. cTnI and cTnI-Ab1 were diluted in 0.01 M (pH = 7.4) PBS solution. Bovine serum albumin (BSA) powder was obtained from Tianjin Kang Yuan Biotechnology Co., Ltd. (Tianjin, China). Bovine serum albumin solution 0.05% was used to dilute cTnI-HRP-Ab2. Ultrasensitive CL kits were obtained from Beijing Labgic Technology Co., Ltd. (Beijing, China). Poly(dimethylsiloxane) (PDMS) and curing agent (Sylgard 184) were from Dow Corning Co., Ltd. (Michigan). The silicone film for coating the cTnI-Ab1 was purchased from Shanghai Shentong Rubber & Plastic Products Co., Ltd. (Shanghai, China). Visualization experiments use a 0.1 M ferric chloride solution and a 0.1 M ammonium thiocyanate standard solution.

The mold used for PDMS chip manufacturing was provided using an AccuFab-L4K light-curing 3D printer from SHINING 3D Technology Co., Ltd. (Hangzhou, China). A 202-00T electric constant-temperature drying oven and a DZF-6020A vacuum-drying oven were purchased from LICHEN-BX Co., Ltd. (Shanghai, China). Bonding of the PDMS chips was performed with a PTL-VM500 plasma cleaner manufactured from Putler Electric Technology Co., Ltd. (Shandong, China). The fluid injection was supplied using an ISPLab02 intelligent syringe pump purchased from Duke Industrial Technology Co., Ltd. (Shanghai, China). The CL image analysis system is acquired from BIO-OI Co., Ltd. (Guangzhou, China). A PH-XDS5 inverted microscope purchased from Phoenix Optical Co., Ltd. (Jiangxi, China) was used to take pictures of fluid mixing during the experiments.

2.2. Mathematical Spiral Structures Parameter Equation. This work investigates three common mathematical spiral equations of Archimedean spiral, Fermat spiral, and hyperbolic spiral. For different mathematical spiral structures, the total arc length of the control channel is 50 mm. Three of the mathematical spiral parametric equations are given in the equation as follows

Archimedean spiral

$$\begin{aligned} x_1 &= 3\cdot t\cdot \sin(t) \\ y_1 &= 3\cdot t\cdot \cos(t) \end{aligned} \quad -2.2 \le t \le 2.3 \tag{1}$$

Fermat spiral

$$\begin{aligned} x_2 &= 0.5\cdot t\cdot \sin(t^2) \\ y_2 &= 0.5\cdot t\cdot \cos(t^2) \end{aligned} \quad 4 \le t \le 3.15\pi \tag{2}$$

Hyperbolic spiral

$$\begin{aligned} x_3 &= 20\cdot \sin(t)/t \\ y_3 &= 20\cdot \cos(t)/t \end{aligned} \quad 2.4 \le t \le 2.4\pi \tag{3}$$

2.3. Numerical Analysis and Simulation. The Navier−Stokes equations are applied on COMSOL Multiphysics to calculate a mixing model for incompressible fluids. We assumed a steady-state flow pattern to simplify the numerical model. The microchannel walls have antislip boundaries. We set the two fluid concentrations at the inlet, and at the outlet, we set the backflow inhibition. A second-order discretization of the dilute matter transfer interface concentrations is used for a more efficient calculation to ensure a more accurate simulation. The Navier−Stokes equations and the convective diffusion equations describe the constant flow in different mathematical spiral mixing channels, incompressible fluids[51]

$$\nabla\cdot\vec{v} = 0 \tag{4}$$

$$\vec{v}\cdot\nabla\vec{v} = -\frac{1}{\rho}\nabla\vec{p} + \nu\nabla^2\vec{v} \tag{5}$$

$$(\vec{v}\nabla)\vec{c} = D_{AB}\nabla^2\vec{c} \tag{6}$$

where ρ denotes the fluid density, $\vec{v}$ denotes the velocity vector, ν represents the kinematic viscosity, p denotes the pressure, and $\vec{c}$ represents the concentration. The simulated fluid density ρ is 10^3 kg/m^3, the diffusion coefficient D_{AB} is 3×10^{-10} m^2·s^{-1}, and the kinematic viscosity ν is 10^{-3} kg/(m·s).

The Re equation, which characterizes fluid flow, is as follows

https://doi.org/10.1021/acsomega.1c05024
ACS Omega 2021, 6, 30779−30789

$$\mathrm{Re} = \frac{\rho v D_h}{\mu} \tag{7}$$

where D_h is the microchannel hydrodynamic diameter. The inlet concentration condition is (0 or 1), the channel walls are slip-free, the outlet pressure synchronizes to 0, and the backflow inhibition is set. The study has chosen an outlet cross section for the mixing performance assessment, n equal parts when griding. The standard deviation calculation of the volume fraction of the components in each cell face assessed the mixing performance. The following equation evaluated the fluid mixing performance.[52]

$$M = \left[1 - \frac{1}{\overline{c_m}}\sqrt{\frac{1}{n}\sum_{i=1}^{n}(c_i - \overline{c_m})^2}\right] \times 100\% \tag{8}$$

where $\overline{c_m}$ is the volume fraction when the fluid is completely mixed, n is the number of points on the cross section, and C_i is the volume fraction at the point i. The fluid is not mixed at all when $M = 0$; when $80\% \leq M < 95\%$, it can be considered that the fluid mixing is well mixed; and when $M \geq 95\%$, the fluid is mixed evenly.

3. METHODOLOGY AND FEASIBILITY VALIDATION

3.1. Numerical Simulation Methods and Grid Independence Tests. Using hydrodynamic theory, we evaluated three mathematical spiral structured micromixers using numerical simulations to grid the geometric model. The grid quality, thickness, and distribution of the nodes all impact the final simulation results. Better grid quality has a more refined grid and reasonable node distribution, which helps numerical simulation results get close to the real values. The grid independence test calculates the results closest to the actual value with the least number of grids before the numerical simulation, reducing the computer calculation time. At the same time, it reduces the requirement of computer configuration and minimizes the waste of resources.

In this work, the grid independence verification uses the Archimedean spiral channel as an example. The COMSOL Multiphysics was used to divide the grid, and design six different tetrahedral structured grids 39 319, 81 725, 181 268, 747 826, 885 493, and 1 039 292, respectively, for numerical simulation calculation. Figure 1 shows the concentration distribution at the centerline of the exit cross section, respectively. As shown in Figure 1, when the grid number is 885 493 or 1039 292, the maximum error of the concentration distribution at the centerline of the cross section is only 0.8%.

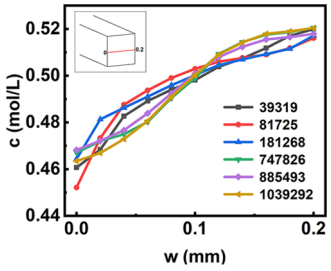

Figure 1. Grid independence tests. The concentration distribution of Archimedean spiral structured micromixers at the centerline of the exit cross section for a total channel arc length of 50 mm, Re = 5, and channel cross section 0.2 mm × 0.2 mm for six different tetrahedral structured grids.

We consider the economic efficiency and choose grid number 885 493 as the grid used for this micromixer simulation. For the Fermat spiral and hyperbolic spiral, micromixer channels were also meshed using the same method.

3.2. Experimental Method and Validation. The actual dimensions of the micromixer channels were measured to verify the reliability of the 3D-printed mold dimensions. Figure 2a–d validates the dimensions for five-channel locations of the Archimedes spiral micromixer. The errors were all below 1.3%, demonstrating the reliability of the 3D printing accuracy.

Then, we verify the consistency of simulation through experiments. The two fluids to be mixed are ferric chloride ($FeCl_3 \cdot 6H_2O$) and ammonium thiocyanate (NH_4SCN) dissolved in deionized water (DI) at the same concentration. The ammonium thiocyanate solution is colorless, and the ferric chloride solution is pale yellow. When these two solutions come into contact, the solution reacts and becomes blood red. The intensity of the red color depicted with the RGB value of each pixel can represent the amount of fluid mixed and react. The normalized intensity of the color indicates the mixing efficiency of the two fluids. In the experiment, the quantification of mixing performance uses concentrations measured in the imaging area of the spiral channel exit section. The mixing efficiency calculation utilizes the pixel intensities of the average RGB values within the imaging area.[53]

$$\eta_{exp} = \frac{I - I_{min}}{I_{max} - I_{min}} \times 100\% \tag{9}$$

where 100% indicates that the two liquids are completely mixed. The value 0 means that the two liquids did not mix at all. I_{max} represents the maximum red intensity observed in the wholly mixed image, and I_{min} defines the minimum intensity observed in the deionized water image. Figure 3 is the simulation and experimental verification of micromixers with different mathematical spiral structures and 3D printing mold diagrams. Figure 3a,c,e shows the comparison between numerical simulations and experimental results for the three mathematical spiral channels at different Re. Figure 3b,d,f shows the 3D-printed mold plots corresponding to the three mathematical spiral structures. As shown in Figure 3a,c,e, the numerical simulation results for the three structures of the micromixer agree with the experimental results, with the maximum error between them being within 5%. There are two primary sources of error. One is that the 3D printing mold process generates surface defects, and therefore the actual microchannels will not be as smooth as in the numerical simulations. The second is that the mixing metrics for the numerical simulation are calculated based on the exit cross section. In contrast, the experimental mixing metrics are calculated based on the top view within the exit imaging area, hence the error between the two.

4. RESULTS AND DISCUSSION

4.1. Effect of Channel Width on the Mixing Performance. Numerical simulation of channels shows the channel widths affect fluid mixing under the same spiral channel length and boundary conditions. As shown in Figure 4, at Re = 5 and a channel width of 0.2 mm, the mixing effect of the Fermat spiral channel is higher than that of the other two mathematical spirals. When the channel width is 0.4 mm, the hyperbolic spiral structure has the best mixing effect, and the

https://doi.org/10.1021/acsomega.1c05024
ACS Omega 2021, 6, 30779−30789

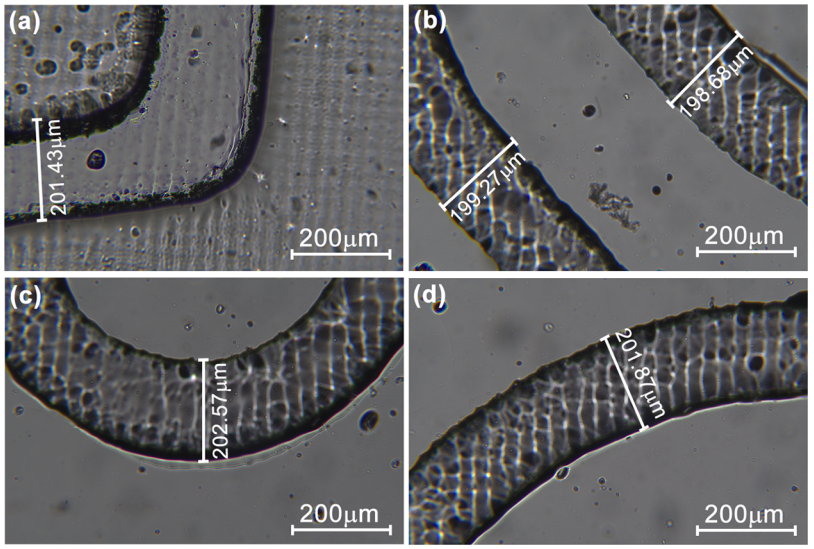

Figure 2. Characterization of the actual dimensions of the channel. (a) Characterization of the dimensions of the Archimedean structured spiral channel at the inlet section. The design width of the inlet section is 200 μm, and the actual size is 201.43 μm, with an error of 0.72%. (b–d) Characterization of the different cross-sectional dimensions of the channel, with a maximum error of 1.29%.

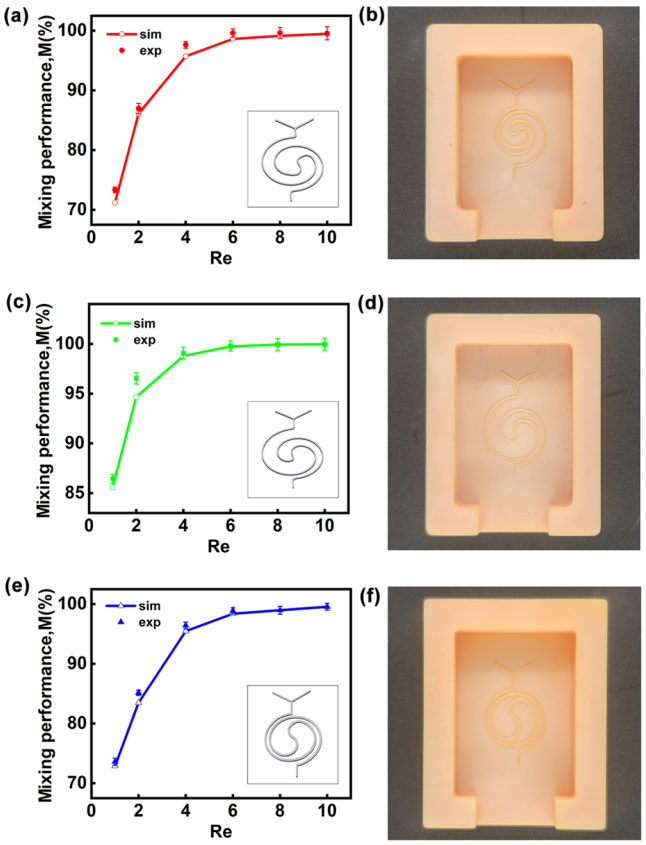

Figure 3. Simulation and experimental verification of micromixers with different mathematical spiral structures and 3D printing mold diagrams. (a, c, e) Numerical simulations and experimental results of Archimedean spiral, Fermat spiral, and hyperbolic spiral at different Re, respectively. (b, d, f) Corresponding 3D-printed molds for the corresponding mathematical spiral structure micromixers; the lengths of the two inlets are 3 and 3 mm, the spiral channel is 50 mm, the outlet is 1.5 mm, and the channel width is 0.2 mm.

Fermat spiral structure has the worst mixing effect. Also, from Figure 4, it can be concluded that the mixing performance

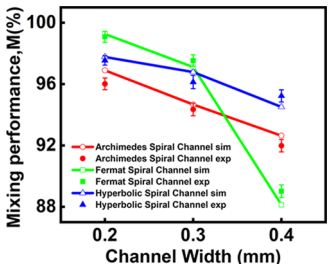

Figure 4. Effect of channel width on mixing performance for three kinds of mathematical spiral structure micromixers with a total channel arc length of 50 mm and Re = 5.

becomes worse as the channel width increases. The mixing efficiency is higher when the channel width is smaller with the fluid flow rate at the same Re. From eq 7, when Re = 5, the smaller the channel width, the greater the flow velocity. Also, the fluid in the channel is in chaotic advection, which increases mixing effectiveness as the flow rate increases.

4.2. Effect of Re on Mixing Performance and Pressure Drop. Molecular diffusion and chaotic advection drive fluid mixing at a microscopic scale. The constant change of curvature radius of the three mathematical spiral structures changes centrifugal forces and facilitates fluid perturbation. In the molecular diffusion-dominated phase, the mixing intensity factor is the total length of the mixing channel. In the chaotic advection-dominated phase, the intensity of Dean vortex is induced by centrifugal force. As shown in Figure 5, at low Re, the dominant factor influencing fluid mixing is molecular diffusion. A lower Re will give a longer time for the fluid diffusion, allowing the molecules to diffuse more thoroughly. Although diffusion of molecules is an inefficient process, the mixing efficiency is not high at the outlet. Figure 5d exhibits, when Re is around 0.4, neither diffusion of molecules nor the chaotic advection dominates the factor. The mixing index at the outlet is the smallest, consequently exhibiting a least effective fluid mixing. With increasing Re, the dominant factor affecting fluid mixing is chaotic advection, and the mixing performance improves with the gradual enhancement of

https://doi.org/10.1021/acsomega.1c05024
ACS Omega 2021, 6, 30779–30789

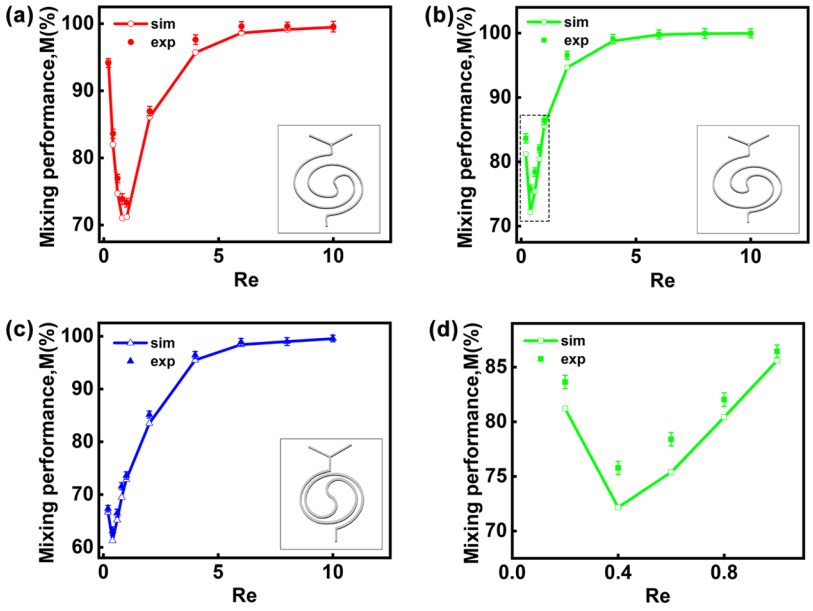

Figure 5. Simulation and experimental mixing performance graphs of different spiral micromixers under different Re. (a−c) Simulation and experimental results of Archimedes, Fermat, and hyperbolic three mathematical spirals at different Re in the channel width of 0.2 mm. (d) Local enlargement of the dashed box area in (b).

chaotic advection. Conversely, chaotic advection is a fast and efficient process. As a result, the fluid mixing performance improves rapidly. Figure 5 shows that the mixing performance of the Fermat spiral structured micromixer is better when the Re is the same. As the Re increases, the mixing index of the fluid at the outlet first decreases and then increases.

Figure 6 shows the fluid simulations and experimental results for a Fermat spiral microchannel micromixer. We used the

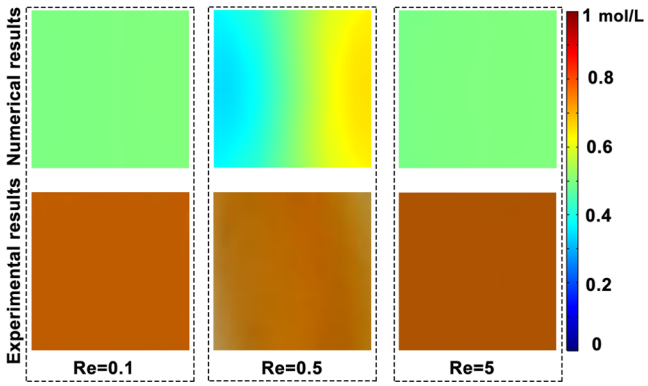

Figure 6. Mixed simulation and experimental results for Fermat spiral channel widths of 0.2 mm and Re = 0.1, 0.5, and 5.

cross section at the outlet to calculate the simulation results. The top view in the imaging area at the outlet shows the experimental results. The fluid simulations agree with the experimental results for varying Re, as shown in Figure 6. The fluid is thoroughly mixed at Re = 0.1 and 5, and at Re = 0.5, the fluid is not thoroughly mixed.

As shown in Figure S1, when the fluid is mixed at a low Re, the maximum pressure drop is about 2×10^3 Pa. Meanwhile, the fluid has been completely mixed, and the pressure drop of the Fermat spiral structure micromixer is the smallest, which is extremely cost-effective.

Through the other two types of micromixers simulation, we compared the pressure drop and mixing performance at four different Re, and the results are shown in Table S1. The pressure drop of the five different micromixers with four different Re is only slightly different. However, the Fermat spiral structure micromixer's pressure drop is the smallest in comparison. The micromixer mixing performance in this work is significantly better than the other two types at low Re, and the Fermat spiral structure micromixer has the highest mixing performance when the fluid is in a chaotic advection state.

4.3. Molecular Diffusion and Chaotic Advection. Using the Fermat spiral structure micromixer as an example, Figure 7 depicts the local mixing pattern of the channels at different Re and different cross sections of concentration. From cross sections A−A to E−E in Figure 7, at Re $\leq$ 0.5, the contact area between the two fluids is confined to the middle of the microchannel when the mixing is dominated by molecular diffusion. The mixing residence time is the key factor affecting molecular diffusion, and the mixing is slow. On the contrary, at Re $\geq$ 5, from cross section A−A and cross section C−C, the fluid is dominated by chaotic advection. Strong Dean vortices form at the cross sections, and the contact area between the two fluids becomes larger, accelerating the mixing of the fluids.

At the cross section D−D, we analyzed the streamlines at two different locations, as shown in Figure 8, where panels (a) and (e), and (b) and (f) are the streamlines at Re = 0.1 and Re = 0.5, respectively. The diagrams show that the streamlines are in parallel with each other, and the curve is smooth. At this time, molecular diffusion mixes the fluid. The mixing of concentration is slow. Panels (c) and (g), and (d) and (h) are, respectively, for Re = 5 and Re = 10 at the two positions of the streamlines diagram. The streamline is no longer parallel. The streamlines are mixed and disordered. Thus, fluid mixing is accelerated, and mixing performance is significantly improved. Figure 9 shows the direction of fluid flow at different Re in five cross sections of the Dean vortices. While Re = 0.1 and Re = 0.2, in this case, the velocity is low, and the mixing of fluid in

https://doi.org/10.1021/acsomega.1c05024
ACS Omega 2021, 6, 30779−30789

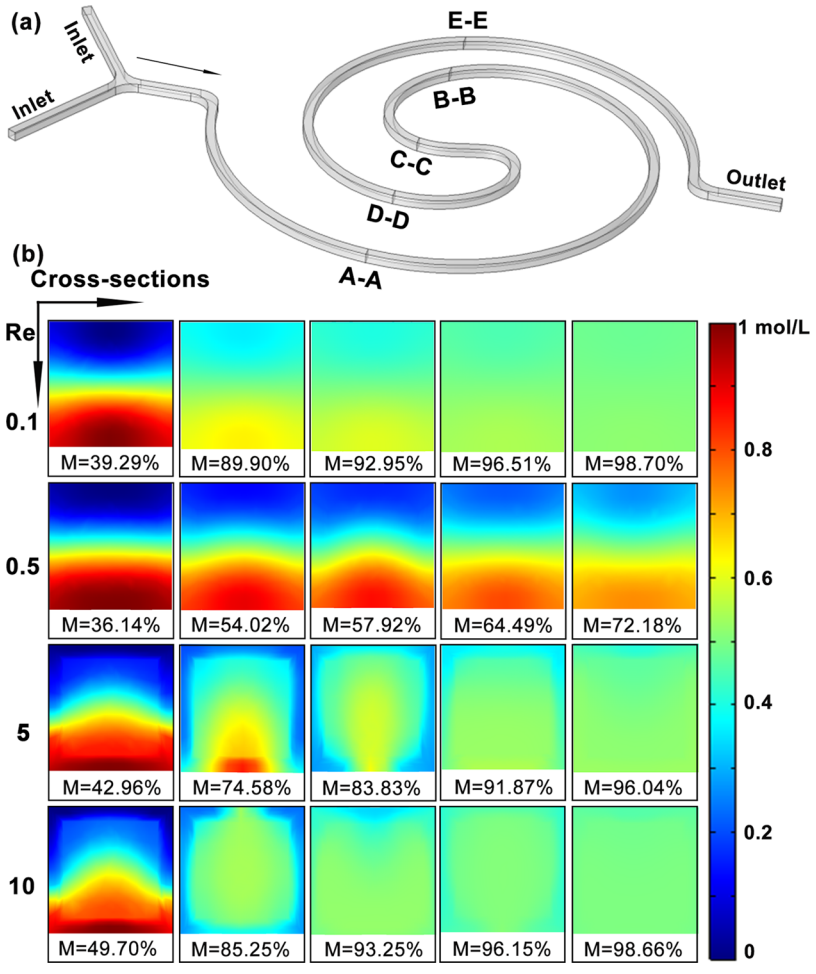

Figure 7. Local mixing patterns of the Fermat spiral micromixer at Re = 0.1, 0.5, 5, and 10. (a) Schematic diagram of Fermat spiral micromixer, including two inlets, one outlet, and five different cross sections. (b) Mixing performance of micromixers at five different cross sections.

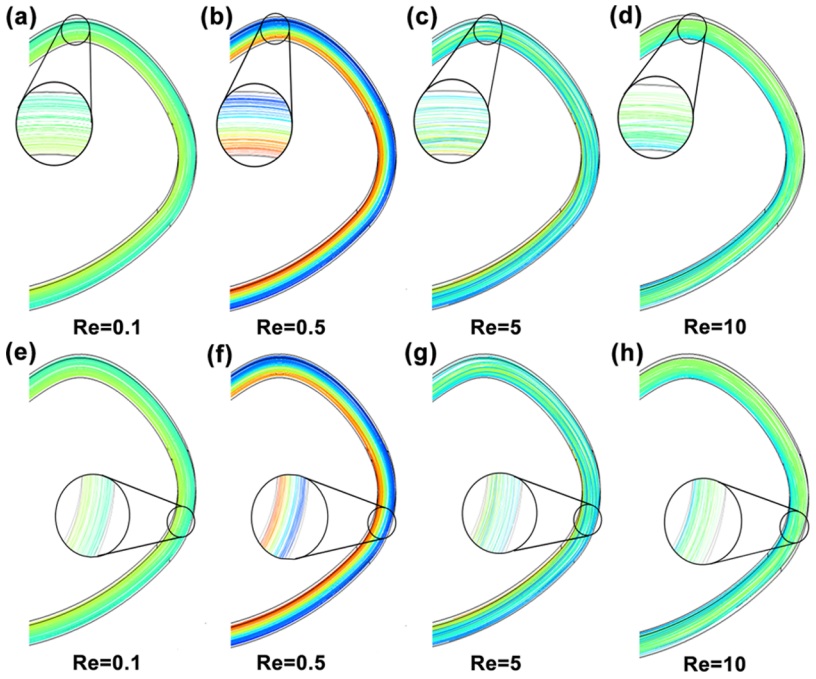

Figure 8. Fermat spiral micromixer at a channel length of 50 mm and a channel width of 0.2 mm; streamline and local magnification at different Re: (a, e) Re = 0.1, (b, f) Re = 0.5, (c, g) Re = 5, (d, h) Re = 10.

https://doi.org/10.1021/acsomega.1c05024
ACS Omega 2021, 6, 30779−30789

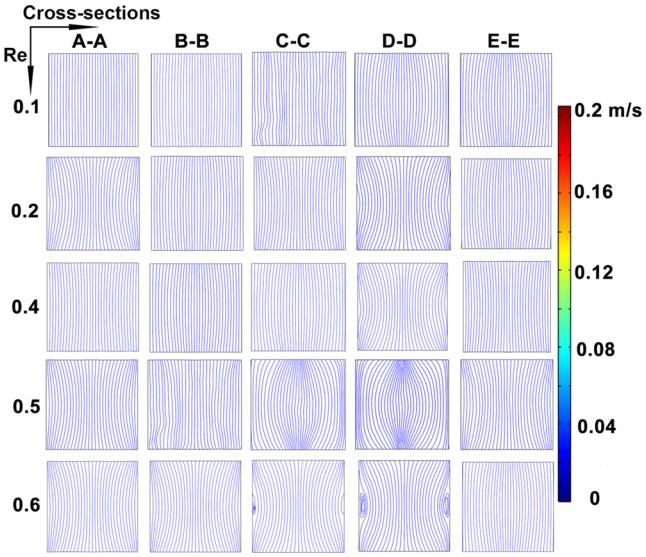

Figure 9. Fermat spiral micromixer at a channel length of 50 mm and a channel width of 0.2 mm, corresponding to the Dean vortices in five cross sections.

the channel is dominated by molecular diffusion. There is no significant vortex generation and the streamlines parallel in the plane. When Re = 0.4, the streamlines are completely parallel and the mixing performance of the fluid is the worst. It can also be seen from Figure 5d. When Re = 0.5 and Re = 0.6, Fermat spiral channel micromixer gradually forms Dean vortices in the C−C and D−D cross sections, and the mixing of fluid in the channel is gradually dominated by chaotic advection. It also deflects the direction of the streamline, and the fluid mixing performance is a continuous improvement.

4.4. Chemiluminescence Immunoassay. We used the Fermat spiral structured micromixer to detect the cTnI. SolidWorks was used to create the components associated with the chip, chip mold, and pressure valve. Exploded views and assembly drawings of the 3D modeling of each component are shown in Figure 10a,b, respectively. An AccuFab-L4K light-curing 3D printer was used to automatically print the chip molds, valves, and other auxiliary parts. The PDMS was 10:1 (mass ratio) mixed with the curing agent, evacuated, and cured. Then, the dual PDMS layer chip in the mold was removed with tweezers, as shown in Figure 10e. Figure 10f shows the complete Fermat spiral microfluidic chip after bonding (60 s of cleaning, power 220 W, gas flow rate 2.0 L/min) and assembly by a plasma cleaner. Figure 10c,d shows the principle of the experimental cTnI assay. The silicone film of the detection area is precoated with one or three cTnI-Ab1 (25 μg/mL) and then precoated with bovine serum albumin. A syringe pump injects cTnI and cTnI-HRP-Ab2, then mixes, and reacts them through the mixing channel. It specifically

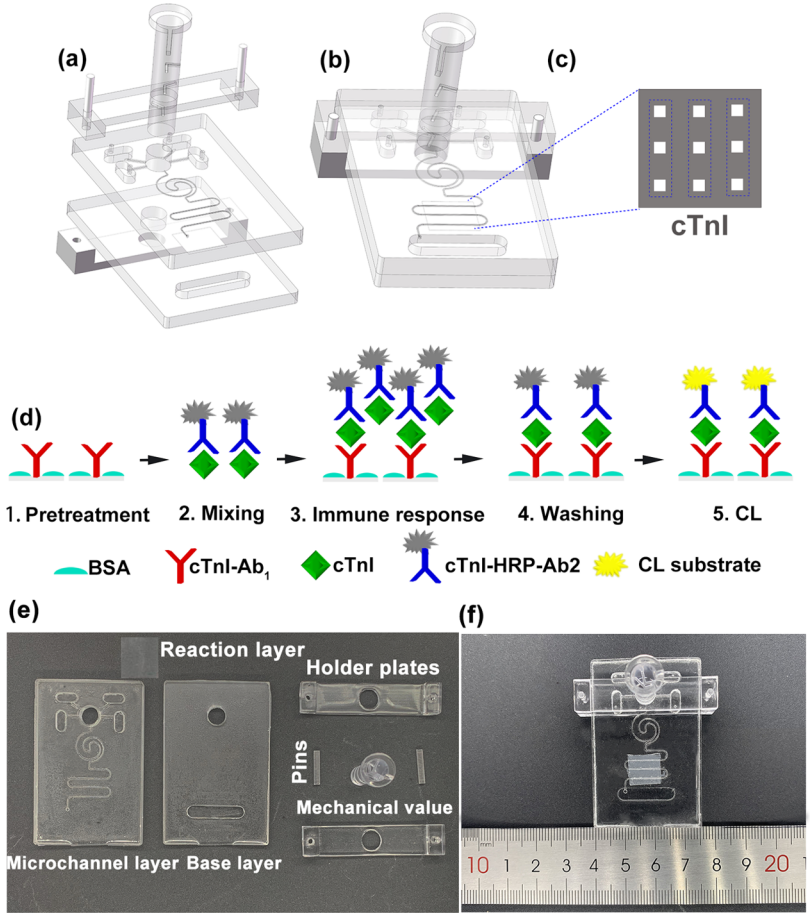

Figure 10. Design and detection principles of microfluidic chips. (a) Exploded view of the three-dimensional modeling of the chip; (b) assembled view; (c) schematic diagram of cTnI-Ab1 in the coating layer; (d) principle of the double-antibody sandwich assay for cTnI; (e) 3D-printed double-layer PDMS chip with pressure valves and other related components; and (f) assembled microfluidic chip.

https://doi.org/10.1021/acsomega.1c05024
ACS Omega 2021, 6, 30779−30789

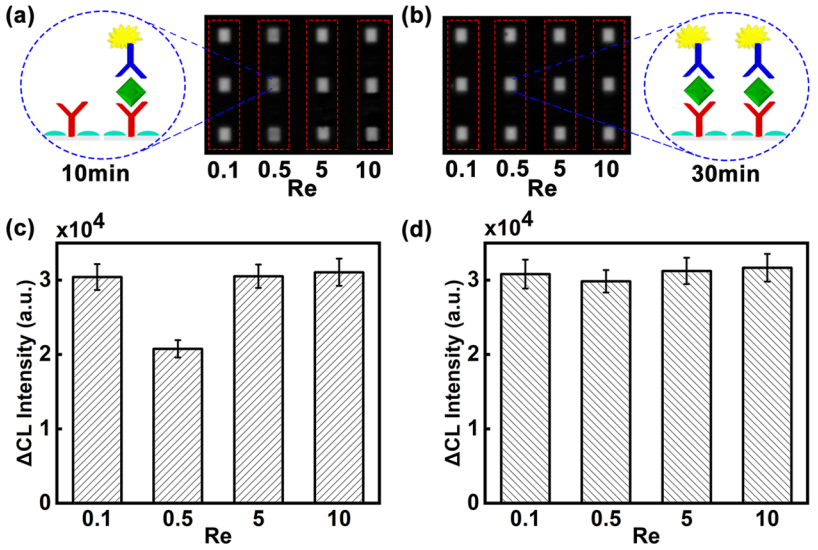

Figure 11. CL dot pattern and the corresponding luminescence intensities at different Re at a cTnI concentration of 1 ng/mL. (a, b) Images of CL fractions at 10 and 30 min incubation, respectively: (a) 10 min incubation and (b) 30 min incubation. (c, d) Corresponding CL intensity at different Re for 10 and 30 min incubation, respectively.

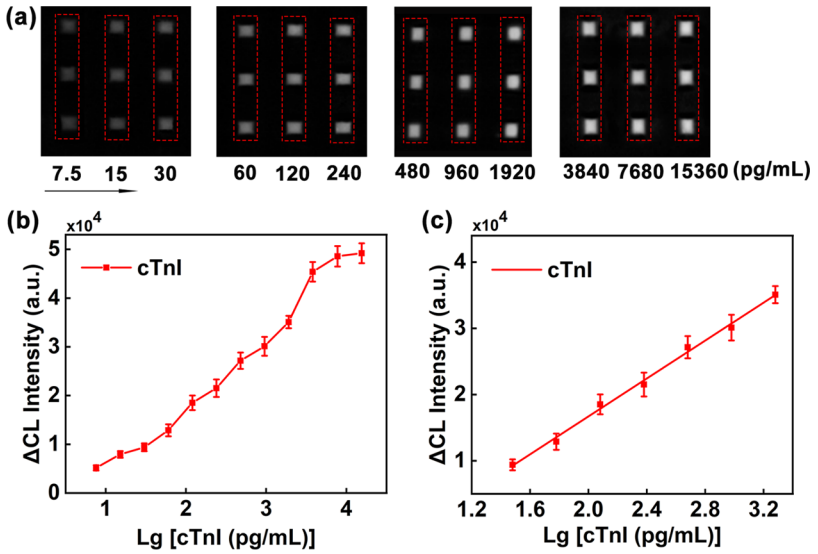

Figure 12. Different concentrations of cTnI CL dot pattern, cTnI detection range, and calibration curve for quantitative analysis. (a) CL dot plot of nine different concentrations of cTnI (concentrations are 7.5, 15, 30, 60, 120, 240, 480, 960, 1920, 3840, 7680, and 15360 pg/ml.). (b) Detection range of cTnI. (c) Standard curve of a specific cTnI concentration.

binds to the cTnI-Ab1 in the detection area to form an immune complex. After incubation, the assay is washed three times with PBS before adding the chemiluminescent substrate.

We precoated a cTnI-Ab1 for the experiments on a silica membrane and set the syringe pump at different flow rates. At different Re, cTnI (1 ng/mL) and cTnI-HRP-Ab2 (2.4 μg/mL) were injected simultaneously into the reaction zone of the chip by the syringe pump via a mixing channel. For POCT purposes, incubation was carried out for 10 min and compared with a complete incubation of 30 min under the same conditions. When the relative standard deviation of the experimental results is greater than 10%, we will re-run the experiment to ensure the accuracy of each assay result. Figure 11a,b shows the images of CL fractions at different incubation times. Figure 11c,d shows the corresponding luminescence intensities at different Re for 10 and 30 min of incubation, respectively. As shown in Figure 11a,b at Re = 0.5, the intensity of CL at 10 min incubation is inferior to that at 30 min incubation, indicating that the two reagents did not mix entirely at this time. To obtain the CL intensity, we subtracted the blank value from the sample value. The blank intensity was tested by adding PBS and measured to be 203.5. Also, at Re = 0.1, 5, and 10, cTnI was mixed and reacted with cTnI-HRP-Ab2 through the spiral channel and then reacted with cTnI-Ab1 in the detection zone. At 10 min of incubation, the CL intensity differed by a maximum of 2.3% from that at 30 min of full incubation, in agreement with the experimental results (Figure 11c,d).

At 10 min incubation and Re = 0.1, 5, and 10, the overall immunoassay times were 18.33, 10.17, and 10.08 min, respectively. Therefore, considering the economic efficiency of the assay, Re $\geq$ 5 is used for detection.

Finally, we verified the detection performance of this micromixer at Re = 5 and 10 min incubation. Before the

https://doi.org/10.1021/acsomega.1c05024
ACS Omega 2021, 6, 30779−30789

experiment, three cTnI-Ab1 were encapsulated in the detection zone and closed with bovine serum albumin. Figure 12b shows a series of standard cTnI concentrations prepared using the micromixer assay with corresponding CL intensity values. The lowest detection limit we detected in the experiment was 7.5 pg/mL. Figure 12a shows the CL dot plots for nine different cTnI concentrations (cTnI, concentration from 7.5 to 15 360 pg/ml). The CL signal is proportional to the concentration of cTnI over a range of concentrations. As shown in Figure 12c, the fitted curves showed good linearity (Y = 14517.18× −12 438.92, R^2 = 0.99) over these concentration ranges (30−1920 pg/mL). The results indicate that this micromixer has high sensitivity in detecting cTnI. When the concentration of cTnI was 30−1920 pg/mL, it showed good linearity (Y = 14517.18× −12438.92, R^2 = 0.99), and the lowest detection limit was 7.5 pg/mL. The assay can be completed in 10 min, meeting the clinical diagnosis needs, and is expecting application in POCT devices.

5. CONCLUSIONS

This work proposes micromixers for low Re mixing using mathematical spiral structures. In the mathematical spiral structure microchannels, the flow direction constantly changes and centrifugal forces induce Dean vortices of different strengths throughout the flow path. We take numerical simulations and visualization experiments to investigate the influence of fluid flow characteristics and mixing performance in the micromixer varying widths of the channel and different Re (0−10). At Re = 5, different channel widths have different effects on the mixing performance of the micromixer and the smaller the channel width, the better the mixing performance. A channel width of 0.2 mm demonstrates the best mixing performance of the Fermat spiral structure micromixer. When the channel width is 0.2 mm, the mixing performance of the three mathematical spiral structure micromixers decreases and then increases as the Re increases. At Re = 5 and the channel width of 0.2 mm, the mixing efficiency of the Fermat spiral structured micromixer reached 99%. We analyzed the streamlines and Dean vortices when the fluid flows. The results show that fluid mixing is mainly based on molecular diffusion if Re ≤ 0.4. However, the molecular residence time is the main factor affecting the mixing performance. Therefore, the mixing is slower. When Re > 0.4, chaotic advection gradually dominates and centrifugal forces induce Dean vortices in the microchannel. This phenomenon causes the contact area to become larger when the fluid mixes and the mixing index increases. We finally integrated a Fermat spiral structured channel into the microfluidic chip and successfully detected an AMI marker using a double-antibody sandwich method. We have successfully shortened the detection time to 10 min. Furthermore, the concentration of cTnI was 30−1920 pg/mL, which showed good linearity (Y = 14 517.18× −12 438.92, R^2 = 0.99), and the lowest detection limit was 7.5 pg/mL. The micromixers showed great potential for use in POCT applications.

■ ASSOCIATED CONTENT

Supporting Information

The Supporting Information is available free of charge at https://pubs.acs.org/doi/10.1021/acsomega.1c05024.

Pressure drop of three mathematical spiral structures micromixers at Re from 0.1 to 10 (Figure S1) and comparison of pressure drop and mixing performance of five different micromixers (Table S1) (PDF)

■ AUTHOR INFORMATION

Corresponding Author

Binfeng Yin − *School of Mechanical Engineering, Yangzhou University, Yangzhou 225127, China;* orcid.org/0000-0002-0484-4951; Email: binfengyin@yzu.edu.cn

Authors

Wenkai Yue − *School of Mechanical Engineering, Yangzhou University, Yangzhou 225127, China*

A. S. M. Muhtasim Fuad Sohan − *School of Mechanical Engineering, Yangzhou University, Yangzhou 225127, China;* orcid.org/0000-0002-0490-1119

Teng Zhou − *Mechanical and Electrical Engineering College, Hainan University, Haikou 570228, China*

Changcheng Qian − *School of Mechanical Engineering, Yangzhou University, Yangzhou 225127, China*

Xinhua Wan − *School of Mechanical Engineering, Yangzhou University, Yangzhou 225127, China*

Complete contact information is available at: https://pubs.acs.org/10.1021/acsomega.1c05024

Author Contributions

B.Y. designed the study, verified the experimental data, and provided funding. W.Y. analyzed the experimental data and drafted the manuscript and graphs. A.S. proofread the manuscript. T.Z. provided funding and carried out the investigation. C.Q. and X.W. edited and validated the manuscript. All authors contributed to the article and approved the submitted version.

Notes

The authors declare no competing financial interest.

■ ACKNOWLEDGMENTS

The authors thank the National Natural Science Foundation of China (grant no. 52075138) and the Natural Science Foundation of Jiangsu Province (grant no. BK20190872) support. They also thank the SHINING 3D Technology Co., Ltd. (Yangzhou and Hangzhou, China) for providing technical support on 3D printing.

■ REFERENCES

(1) Lee, C. Y.; Wang, W. T.; Liu, C. C.; Fu, L. M. Passive mixers in microfluidic systems: A review. *Chem. Eng. J.* **2016**, *288*, 146−160.

(2) Haeberle, S.; Zengerle, R. Microfluidic platforms for lab-on-a-chip applications. *Lab Chip* **2007**, *7*, 1094−1110.

(3) Thiele, M.; Knauer, A.; Malsch, D.; Csaki, A.; Henkel, T.; Kohler, J. M.; Fritzsche, W. Combination of microfluidic high-throughput production and parameter screening for efficient shaping of gold nanocubes using Dean-flow mixing. *Lab Chip* **2017**, *17*, 1487−1495.

(4) Sudarsan, A. P.; Ugaz, V. M. Fluid mixing in planar spiral microchannels. *Lab Chip* **2006**, *6*, 74−82.

(5) Jeong, G. S.; Chung, S.; Kim, C. B.; Lee, S. H. Applications of micromixing technology. *Analyst* **2010**, *135*, 460−473.

(6) Elvira, K. S.; Solvas, X. C. I.; Wootton, R. C. R.; deMello, A. J. The past, present and potential for microfluidic reactor technology in chemical synthesis. *Nat. Chem.* **2013**, *5*, 905−915.

(7) Bessoth, F. G.; deMello, A. J.; Manz, A. Microstructure for efficient continuous flow mixing. *Anal. Commun.* **1999**, *36*, 213−215.

(8) Melin, J.; Gimenez, G.; Roxhed, N.; van der Wijngaart, W.; Stemme, G. A fast passive and planar liquid sample micromixer. *Lab Chip* **2004**, *4*, 214−219.
(9) Lee, C. Y.; Fu, L. M. Recent advances and applications of micromixers. *Sens. Actuators, B* **2018**, *259*, 677−702.
(10) Cai, G. Z.; Xue, L.; Zhang, H. L.; Lin, J. H. A Review on Micromixers. *Micromachines* **2017**, *8*, 274−300.
(11) Zhang, C. S.; Xing, D.; Li, Y. Y. Micropumps, microvalves, and micromixers within PCR microfluidic chips: Advances and trends. *Biotechnol. Adv.* **2007**, *25*, 483−514.
(12) Chen, J. K.; Weng, C. N.; Yang, R. J. Assessment of three AC electroosmotic flow protocols for mixing in microfluidic channel. *Lab Chip* **2009**, *9*, 1267−1273.
(13) Huang, M. C.; Ye, H.; Kuan, Y. K.; Li, M. H.; Ying, J. Y. Integrated two-step gene synthesis in a microfluidic device. *Lab Chip* **2009**, *9*, 276−285.
(14) Yesiloz, G.; Boybay, M. S.; Ren, C. L. Effective Thermo-Capillary Mixing in Droplet Microfluidics Integrated with a Microwave Heater. *Anal. Chem.* **2017**, *89*, 1978−1984.
(15) Modarres, P.; Tabrizian, M. Phase-controlled field-effect micromixing using AC electroosmosis. *Microsyst. Nanoeng.* **2020**, *6*, No. 60.
(16) Yu, S.; Jeon, T. J.; Kim, S. M. Active micromixer using electrokinetic effects in the micro/nanochannel junction. *Chem. Eng. J.* **2012**, *197*, 289−294.
(17) Fu, X.; Liu, S. F.; Ruan, X. D.; Yang, H. Y. Research on staggered oriented ridges static micromixers. *Sens. Actuators, B* **2006**, *114*, 618−624.
(18) Serra, C.; Sary, N.; Schlatter, G.; Hadziioannou, G.; Hessel, V. Numerical simulation of polymerization in interdigital multilamination micromixers. *Lab Chip* **2005**, *5*, 966−973.
(19) Kim, S. J.; Wang, F.; Burns, M. A.; Kurabayashi, K. Temperature-Programmed Natural Convection for Micromixing and Biochemical Reaction in a Single Microfluidic Chamber. *Anal. Chem.* **2009**, *81*, 4510−4516.
(20) Mair, D. A.; Schwei, T. R.; Dinio, T. S.; Svec, F.; Frechet, J. M. J. Use of photopatterned porous polymer monoliths as passive micromixers to enhance mixing efficiency for on-chip labeling reactions. *Lab Chip* **2009**, *9*, 877−883.
(21) Rezk, A. R.; Qi, A.; Friend, J. R.; Li, W. H.; Yeo, L. Y. Uniform mixing in paper-based microfluidic systems using surface acoustic waves. *Lab Chip* **2012**, *12*, 773−779.
(22) Xia, H. M.; Wan, S. Y. M.; Shu, C.; Chew, Y. T. Chaotic micromixers using two-layer crossing channels to exhibit fast mixing at low Reynolds numbers. *Lab Chip* **2005**, *5*, 748−755.
(23) Lok, K. S.; Kwok, Y. C.; Nam-Trung, N. Double spiral detection channel for on-chip chemiluminescence detection. *Sens. Actuators, B* **2012**, *169*, 144−150.
(24) Yang, J.; Qi, L.; Chen, Y.; Ma, H. Design and Fabrication of a Three Dimensional Spiral Micromixer. *Chin. J. Chem.* **2013**, *31*, 209−214.
(25) Xiang, N.; Li, Q.; Shi, Z. G.; Zhou, C. G.; Jiang, F. T.; Han, Y.; Ni, Z. H. Low-cost multi-core inertial microfluidic centrifuge for high-throughput cell concentration. *Electrophoresis* **2020**, *41*, 875−882.
(26) Xiang, N.; Ni, Z. Electricity-free hand-held inertial microfluidic sorter for size-based cell sorting. *Talanta* **2021**, *235*, 122807−122814.
(27) Xiang, N.; Wang, S. L.; Ni, Z. H. Secondary-flow-aided single-train elastic-inertial focusing in low elasticity viscoelastic fluids. *Electrophoresis* **2021**, DOI: 10.1002/elps.202100086.
(28) Hossain, S.; Kim, K. Y. Mixing Performance of a Serpentine Micromixer with Non-Aligned Inputs. *Micromachines* **2015**, *6*, 842−854.
(29) Vatankhah, P.; Shamloo, A. Parametric study on mixing process in an in-plane spiral micromixer utilizing chaotic advection. *Anal. Chim. Acta* **2018**, *1022*, 96−105.
(30) Wang, X.; Liu, Z.; Cai, Y.; Wang, B.; Luo, X. A cost-effective serpentine micromixer utilizing ellipse curve. *Anal. Chim. Acta* **2021**, *1155*, No. 338355.
(31) Yin, B.; Qian, C.; Wang, S.; Wan, X.; Zhou, T. A Microfluidic Chip-Based MRS Immunosensor for Biomarker Detection via Enzyme-Mediated Nanoparticle Assembly. *Front. Chem.* **2021**, *9*, No. 688442.
(32) Liu, W. T.; Zhu, L.; Qin, Q. W.; Zhang, Q.; Feng, H. H.; Ang, S. Microfluidic device as a new platform for immunofluorescent detection of viruses. *Lab Chip* **2005**, *5*, 1327−1330.
(33) Hu, J.; Wang, S. Q.; Wang, L.; Li, F.; Pingguan-Murphy, B.; Lu, T. J.; Xu, F. Advances in paper-based point-of-care diagnostics. *Biosens. Bioelectron.* **2014**, *54*, 585−597.
(34) Regehr, K. J.; Domenech, M.; Koepsel, J. T.; Carver, K. C.; Ellison-Zelski, S. J.; Murphy, W. L.; Schuler, L. A.; Alarid, E. T.; Beebe, D. J. Biological implications of polydimethylsiloxane-based microfluidic cell culture. *Lab Chip* **2009**, *9*, 2132−2139.
(35) Yin, B.; Zheng, W.; Dong, M.; Yu, W.; Chen, Y.; Joo, S. W.; Jiang, X. An enzyme-mediated competitive colorimetric sensor based on Au@Ag bimetallic nanoparticles for highly sensitive detection of disease biomarkers. *Analyst* **2017**, *142*, 2954−2960.
(36) Chen, Y.; Yin, B.; Dong, M.; Xianyu, Y.; Jiang, X. Versatile T-1-Based Chemical Analysis Platform Using Fe3+/Fe2+ Interconversion. *Anal. Chem.* **2018**, *90*, 1234−1240.
(37) Liu, J.; Geng, Z.; Fan, Z.; Liu, J.; Chen, H. Point-of-care testing based on smartphone: The current state-of-the-art (2017-2018). *Biosens. Bioelectron.* **2019**, *132*, 17−37.
(38) Yin, B.; Wan, X.; Qian, C.; Sohan, A.; Wang, S.; Zhou, T. Point-of-Care Testing for Multiple Cardiac Markers Based on a Snail-Shaped Microfluidic Chip. *Front. Chem.* **2021**, *9*, No. 741058.
(39) Xia, Y.; Si, J.; Li, Z. Fabrication techniques for microfluidic paper-based analytical devices and their applications for biological testing: A review. *Biosens. Bioelectron.* **2016**, *77*, 774−789.
(40) Axelrod, T.; Eltzov, E.; Marks, R. S. Capture-Layer Lateral Flow Immunoassay: A New Platform Validated in the Detection and Quantification of Dengue NS1. *Acs Omega* **2020**, *5*, 10433−10440.
(41) Yin, B.; Wang, Y.; Dong, M.; Wu, J.; Ran, B.; Xie, M.; Joo, S. W.; Chen, Y. One-step multiplexed detection of foodborne pathogens: Combining a quantum dot-mediated reverse assaying strategy and magnetic separation. *Biosens. Bioelectron.* **2016**, *86*, 996−1002.
(42) Choi, K.; Ng, A. H. C.; Fobel, R.; Chang-Yen, D. A.; Yarnell, L. E.; Pearson, E. L.; Oleksak, C. M.; Fischer, A. T.; Luoma, R. P.; Robinson, J. M.; Audet, J.; Wheeler, A. R. Automated Digital Microfluidic Platform for Magnetic-Particle-Based Immunoassays with Optimization by Design of Experiments. *Anal. Chem.* **2013**, *85*, 9638−9646.
(43) Chan, H. N.; Tan, M. J. A.; Wu, H. Point-of-care testing: applications of 3D printing. *Lab Chip* **2017**, *17*, 2713−2739.
(44) Amin, R.; Knowlton, S.; Hart, A.; Yenilmez, B.; Ghaderinezhad, F.; Katebifar, S.; Messina, M.; Khademhosseini, A.; Tasoglu, S. 3D-printed microfluidic devices. *Biofabrication* **2016**, *8*, 022001−022017.
(45) Comina, G.; Suska, A.; Filippini, D. PDMS lab-on-a-chip fabrication using 3D printed templates. *Lab Chip* **2014**, *14*, 424−430.
(46) Waheed, S.; Cabot, J. M.; Macdonald, N. P.; Lewis, T.; Guijt, R. M.; Paull, B.; Breadmore, M. C. 3D printed microfluidic devices: enablers and barriers. *Lab Chip* **2016**, *16*, 1993−2013.
(47) Hossain, S.; Ansari, M. A.; Kim, K. Y. Evaluation of the mixing performance of three passive micromixers. *Chem. Eng. J.* **2009**, *150*, 492−501.
(48) Mariotti, A.; Galletti, C.; Mauri, R.; Salvetti, M. V.; Brunazzi, E. Steady and unsteady regimes in a T-shaped micro-mixer: Synergic experimental and numerical investigation. *Chem. Eng. J.* **2018**, *341*, 414−431.
(49) Zhou, F.; Lu, M.; Wang, W.; Bian, Z. P.; Zhang, J. R.; Zhu, J. J. Electrochemical Immunosensor for Simultaneous Detection of Dual Cardiac Markers Based on a Poly(Dimethylsiloxane)-Gold Nanoparticles Composite Microfluidic Chip: A Proof of Principle. *Clin. Chem.* **2010**, *56*, 1701−1707.
(50) Lok, K. S.; Kwok, Y. C.; Nguyen, N. T. Passive micromixer for luminol-peroxide chemiluminescence detection. *Analyst* **2011**, *136*, 2586−2591.

https://doi.org/10.1021/acsomega.1c05024
ACS Omega 2021, 6, 30779−30789

(51) Cheri, M. S.; Latifi, H.; Moghaddam, M. S.; Shahraki, H. Simulation and experimental investigation of planar micromixers with short-mixing-length. *Chem. Eng. J.* **2013**, *234*, 247−255.
(52) Ansari, M. A.; Kim, K. Y. Parametric study on mixing of two fluids in a three-dimensional serpentine microchannel. *Chem. Eng. J.* **2009**, *146*, 439−448.
(53) Hsu, C. W.; Shih, P. T.; Chen, J. M. Enhancement of Fluid Mixing with U-Shaped Channels on a Rotating Disc. *Micromachines* **2020**, *11*, 1110−1129.

NOTE ADDED AFTER ASAP PUBLICATION

Due to production errors, the version of this paper that was published ASAP November 2, 2021, contained errors in three equations. The errors were corrected, and the revised version was reposted November 3, 2021.

https://doi.org/10.1021/acsomega.1c05024
ACS Omega 2021, 6, 30779−30789